Regular Article

Influence of container shape and size on surface-tension-driven Bénard convection

M. Medale[a] and P. Cerisier

Aix Marseille Université, CNRS, IUSTI UMR 7343, 13453 Marseille, France

Abstract. The aim of this study is to investigate the influence of the container size and shape on the main fluid flow characteristics of Surface-Tension-Driven Bénard Convection. Computations have been performed for high Prandtl number fluids and realistic boundary conditions in various configurations either at steady state when it exists or unsteady one for $Ma_c \leq Ma \leq 2.5Ma_c$. The threshold value, its associated pattern and secondary bifurcation one are presented for each configuration. For very small aspect ratios, it turns out that the threshold value is determined by the friction coefficient whereas for medium size aspect ratios both size and shape enters the game in a more subtle way. Some containers have been found to induce a quasi-perfect hexagonal pattern in their core region provided they satisfy shape and size compatibility conditions. Otherwise, dynamical regimes may appear even close to the threshold so their peculiar characteristics have been reported and analyzed as they seem to be intrinsic to small aspect ratio configurations.

1 Introduction

Natural convection has been extensively studied during the last few decades, because of its practical importance and theoretical relevance. Buoyancy and surface tension both take place in a wide range of industrial applications in which convection play a crucial part and must be controlled to end up in high quality processes (coating, painting, welding, etc.). In this paper we are interested in the cases where buoyancy is negligible with respect to surface tension gradients, the so-called Surface-Tension-Driven Bénard Convection ($STDBC$). The main feature of this configuration is such that for a fluid layer of large horizontal extension the convective flow is organized into a cellular pattern just above the threshold, the famous hexagonal pattern first studied by Bénard [1]. On the other hand when the liquid is confined into small containers, mechanical and thermal effects of lateral walls become determining so that vessel size and shape strongly affect the fluid flow pattern. Most of its characteristics are very different from the infinite layer case owing to the imposed physical and geometrical restraints.

[a] e-mail: marc.medale@univ-amu.fr

The literature on confined $STDBC$ is scarce and scattered [5,18] and yield a variety of results somehow disconnected owing to various operating conditions and driving physical mechanisms at play. They are characterized by at least four dimensionless numbers (Rayleigh, Marangoni, Biot, Prandtl), container size and shape, etc. The influence of the aspect ratio on the pattern characteristics in Rayleigh-Bénard-Marangoni convection confined into hexagonal and triangular vessels of various sizes was first reported in [2,3]. Then, many other experiments were performed in circular and square containers of small aspect ratios for $STDBC$ [14]. Linear stability analyses were also performed in confined configurations (square and rectangular enclosures [10], circular ones [8,24]. Pattern transitions and unsteady behaviours have been studied in some peculiar small vessel cases. A dynamical four-cell pattern has been observed in a small aspect ratio square container at large distance from the threshold for which dynamical models have been derived [15,19] and references therein. Comparable dynamical behaviors were also observed in small aspect ratio circular containers [11,13] and later on modeled and analyzed [6].

The aim of the present study is to investigate the influence of the container shape and size for $STDBC$ on: i) the threshold value and its associated pattern; ii) the steady or unsteady convective fluid flow pattern beyond the threshold up to the secondary bifurcation. The content of the paper is as follows. Section 2 briefly presents physical assumptions, governing equations and implemented numerical model. The influence of the container shape and size on the convective threshold value and its associated patternalong with steady states at second bifurcation are presented in Sect. 3, while dynamical regimes are presented in Sect. 4. A discussion on some generic features is provided in Sect. 5 and a summary is given in Sect. 6.

2 Physical and numerical models

Our study deals with $STDBC$ in an horizontal liquid layer for which the liquid-air interface is assumed to be flat (no meniscus), the heat transfer across the thin air layer is dominated by conduction (Biot number $Bi < 0.5$), it is bounded by below by a hot isothermal wall and surrounded by an adiabatic lateral wall. This latter assumption mimics experimental configurations in presence of an outer liquid guard ring [14]. Taking into account these assumptions and recalling that we are interested in the weakly non-linear regime led us to consider a one layer model, which has been confirmed to be very satisfactory in the considered case [12]. Under these assumptions the problem is governed by the coupled incompressible Navier-Stokes and energy equations, under the Boussinesq approximation. Introducing dimensionless variables of space, time, velocity (V), pressure (p) and temperature (θ), d_l, d_l^2/κ, κ/d_l and ΔT respectively into the conservation equations of mass, momentum and energy equations read:

$$\boldsymbol{\nabla} \cdot \mathbf{V} = 0 \tag{1}$$

$$\frac{1}{Pr}\left(\frac{\partial \mathbf{V}}{\partial t} + \mathbf{V} \cdot \nabla \mathbf{V}\right) = -\boldsymbol{\nabla}p + \Delta\mathbf{V} + Ra\,\theta\,\boldsymbol{e_z} \tag{2}$$

$$\frac{\partial \theta}{\partial t} + \mathbf{V} \cdot \boldsymbol{\nabla}\theta = \Delta\theta \tag{3}$$

supplemented with appropriate initial and boundary conditions. The fluid flow boundary conditions are no slip velocity at solid walls ($\mathbf{V} = 0$) and the Marangoni condition at the free surface ($z = 1$): $\mathbf{V}\cdot\mathbf{n} = 0$; $\frac{\partial u}{\partial z} = -Ma\frac{\partial \theta}{\partial x}$ and $\frac{\partial v}{\partial z} = -Ma\frac{\partial \theta}{\partial y}$. The associated heat transfer boundary conditions reduce to $\theta = 1$ at the heated horizontal bottom wall ($z = 0$), $\frac{\partial \theta}{\partial n} = 0$ at all lateral walls, and $\frac{\partial \theta}{\partial n} = -Bi\theta$ at the free surface ($z = 1$).

The related physical parameters have been gathered into four non-dimensional numbers, namely the Biot number ($Bi = \frac{d_l}{\kappa_l}\frac{\kappa_a}{d_a}$), the Marangoni number ($Ma = \frac{\gamma d_l \Delta T}{\mu_l \kappa_l}$), the Rayleigh number ($Ra = \frac{\beta g d_l^3 \Delta T}{\nu_l \kappa_l}$) and the Prandtl number ($Pr = \nu_l/\kappa_l$). They involve eleven physical quantities, namely $d_l, d_a, k_l, k_a, g, \beta, \gamma, \kappa, \nu_l, \mu_l, \Delta T$, representing liquid and air layer thickness, liquid and air thermal conductivity coefficients, coefficient of gravitational acceleration, temperature coefficients of density and surface-tension, thermal diffusivity, kinematic and dynamic viscosity of the liquid, average temperature difference across the liquid layer, respectively. On the other hand, in order to compare vessels having different shapes we also introduce an extra non-dimensional number, the aspect ratio defined as $\Gamma = \sqrt{A}/d_l$, where A represents the free surface area.

Reference computations in $STDBC$ have been conducted in the past, but none of them simultaneously account for effective presence of lateral walls, critical and fully developed convection, etc. [12, 20, 21]. The numerical model we have developed aims to overcome most of the above mentioned limitations. It enables us to compute the threshold value and its associated pattern, fully non linear steady states or transient solutions for containers of various shapes (polygonal or circular) and small-to-moderate horizontal extension. The numerical model dealing with the unsteady solution algorithm is presented in [16], whereas the steady state solution algorithm along with the continuation one enabling us to locate the threshold and subsequent bifurcations have been described in [4, 17]. Various validations on $STDBC$ configurations have been conducted successfully on both experimental and numerical references solutions. The set of chosen dimensionless parameters refer to a silicone oil layer ($Pr = 900$), considered in the $STDBC$ limit ($Ra = 0$), topped by a thin air layer ($Bi = 0.1$) into containers of various shapes (regular polygons from 3 to 6 lateral sides and circular), of various sizes. The considered Γs (from 2 up to 24) were selected either for comparison purposes [14] or with respect to the size compatibility condition, hereafter defined. Geometrical characteristics are gathered in appendix, along with computational meshes.

3 Container size and shape influence on threshold and its pattern

The container shapes have been chosen by virtue of their expected geometrical compatibility or incompatibility with respect to the perfect hexagonal pattern. Equilateral triangle and regular hexagonal containers should a priori conform to the basic $STDBC$ hexagonal pattern, so in the following they are classified as compatible vessels (CV). On the other hand regular pentagon and square or rectangular containers are expected to be incompatible vessels (ICV), meanwhile the circular containers represent a special case owing to their axial symmetry. In the following P_n designates regular polygon with n side walls ($3 \leq n \leq 6$) and P_∞ circular vessel, respectively. According to the authors' knowledge, there are neither threshold values nor patterns reported in the literature for P_3, P_5 and P_6, whereas for P_4 or P_∞ they are scarce and do not necessarily correspond to our physical parameters. Several comparisons have been nevertheless made in the case of square vessels with $\Gamma = 2$, where we found $Ma_c = 145.4$ ($Bi = 0.1$), which is in good agreement with 145.8, 146.1 and 145.8 reported in [7, 9, 23] ($Bi = 1$), respectively. For $\Gamma = 5.70, 6.19, 6.37, 8.45, 9.70$ the discrepancy between our threshold values and those of Dauby et al. [8] ($Bi = 1$) never exceeds 1.5%. Likewise for circular vessels we found $Ma_c = 87.6$ for $\Gamma = 4.71$ (for $Bi = 0.1, Pr = 900$) whereas interpolation of Fig. 1 from Dauby et al. [7] gives 86.6 ($Bi = 0, Pr = 10^4$), which is consistent with the Biot number difference. Our values are also within 2% as compred to that of Dauby et al. [8] for $Bi = 1$, which is consistent with the fact that Ma_c increases with Bi (see for instance [24]).
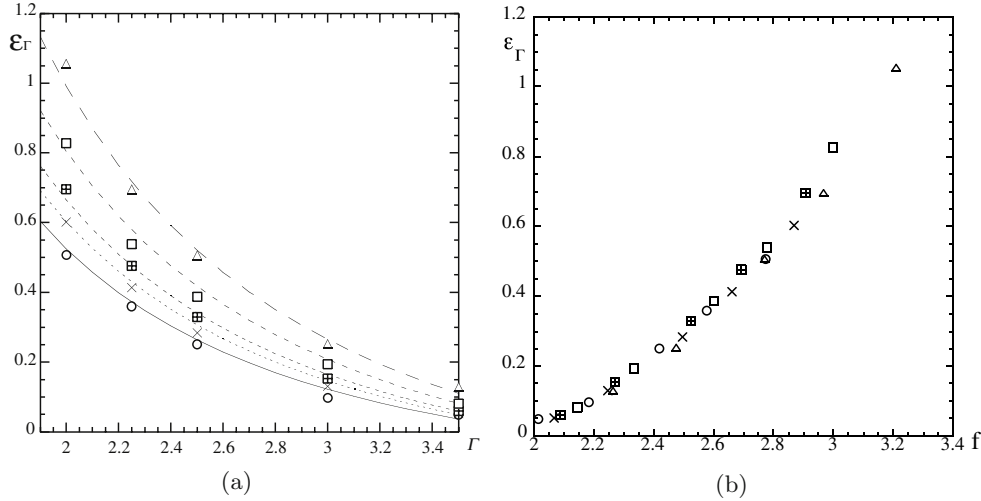
Fig. 1. Relative threshold values in very small aspect ratio containers of various shapes, for $Pr = 900, Bi = 0.1$ (legend: $\triangle$ P_3; $\square$ P_4; $\boxplus$ P_5; x P_6; $\circ$ P_∞). (a) Versus aspect ratio (Γ) and from suggested correlation Eq. (4); (b) versus friction coefficient (f).

Thresholds are numerically detected when the algebraic system becomes singular [4]. We have plotted in Fig. 1a and Fig. 2 (plain symbols) the relative distance of the critical Marangoni number (Ma_c) for the considered containers with respect to the limiting case of infinite horizontal extension ($Ma_{c\infty}$), versus the aspect ratio. Figure 1a gathers the very-small aspect ratio range ($\Gamma < 3.5$), because there is only one cell in the pattern. Figures 2a–e gather the small-to-medium range $3.5 < \Gamma < 24$, where the pattern consists of more than one cell. As expected, the Ma_c in finite size containers are always larger than the infinite layer value ($Ma_{c\infty}$) owing to the lateral confinement and the resulting no-slip boundary condition. In very small aspect ratios only one cell fills the vessel and takes roughly its shape (less than 3% of the free surface is motionless in the wedge vicinity for P_3). Ma_c steeply increases as Γ decreases for a given vessel shape (size effect). On the other hand for a given Γ the threshold value slightly increases as the vessel wetted surface increases (i.e. from P_∞ to P_3 containers) (shape effect). In small-to-medium vessels several cells can fill the container. The dotted lines in Fig. 2 only serve as guides to the eye since the threshold line can exhibit non-monotonic variation between selected Γ values. A slight slope breaking appears in the range $7 < \Gamma < 9$, which corresponds to the first core-cell that appears in the pattern and indicates the transition from the small to medium aspect ratio configurations. For $\Gamma > 10$ the threshold asymptotically approaches $Ma_{c\infty}$ (less than 2% for $\Gamma > 20$).

At threshold the convective pattern induced in a container results from two independent constraints. The first one comes from lateral walls, which directly induces an orientation or shape constraint to the pattern as the cell-side separating two adjacent cells lying along a lateral wall is roughly perpendicular to it. The second one is a size constraint that originates from cellular convection in the bulk, which seeks to set in at the same time in the whole fluid layer as a rather regular tiling of the plane. Hence, if the pattern reconcile these two constraints it results in a quasi-perfect hexagonal pattern for large enough Γ, whereas otherwise structural defects appear. One can then define the container shape compatibility (or incompatibility) as the ability (or inability) for a given container to induce a quasi-perfect hexagonal steady state pattern.
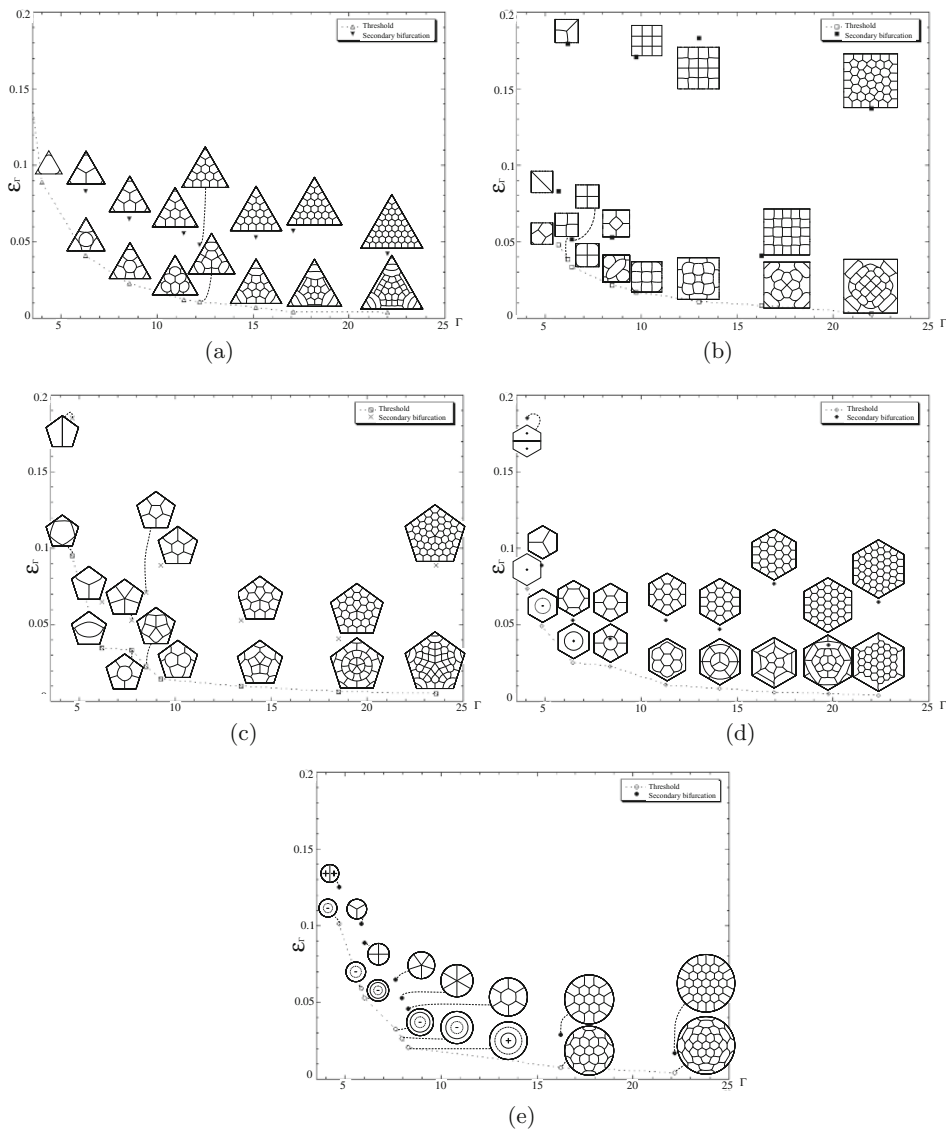
Fig. 2. Thresholds (open symbols), patterns at threshold (lower row), secondary bifurcations (bold symbols) and patterns at secondary bifurcation (upper row) in various shape containers: (a) triangular; (b) square; (c) pentagonal; (d) hexagonal; (e) circular.

Besides the evolution of Ma_c versus Γ, Fig. 2 also presents a synopsis of the associated convective patterns at threshold (lower row, plain symbols) and at second bifurcation (upper row, bold symbols). Solid lines represent the cell limits at free surface, which correspond to a zero horizontal velocity component. When not specified the flow is upward in the cell centre and downward along its periphery, otherwise "+" or "−" signs indicate specific upward or downward flows. Finally, a dashed line indicates the separating line at the free surface between convective adjacent torus. Very few patterns are available in literature for the Γ considered, but when they exist the agreement is good. Furthermore, patterns at threshold are very difficult to observe experimentally owing to the very small value of velocity. Moreover a secondary steady

state bifurcation could also occur very close to the threshold and it could be sometimes mistaken with the former by experimentalists. The general trend is that the pattern is made of different kinds of convective cells with cell edges not always straight line. Computations show that cells of highest kinetic energy tend to have a concave regular boundary, whilst conversely cells of lower kinetic energy have a convex boundary and finally boundary between cells of similar energy levels is straight. Finally it is noteworthy that hexagonal cells never appear (in the range of studied Γ) immediately at the threshold in the ICVs (P_4 and P_5) whereas they appear in CVs for $\Gamma > 8$ in P_3 and for $\Gamma > 11$ in P_6, but with curved cell sides. Considering the correspondence between pattern and vessel symmetries one can observe that the container most often imposes only some of its own symmetries. Indeed, apart patterns in P_3 that always keep its three-fold symmetry whatever Γ is, all others loose for some aspect ratios some of the vessel symmetries. Furthermore, from obtained results and to unify denominations among authors, one can suggest a classification of container sizes relevant to confined configurations. Let N_{lc} and N_{cc} designate the numbers of lateral and core cells in a steady-state pattern, respectively. Five ranges of aspect ratios are distinguished according to their intrinsic convective pattern structure:

- $N_{lc} = 1$ and $N_{cc} = 0$: $\Gamma < 3.5$; very small aspect ratios (VS);
- $N_{lc} > 1$ and $N_{cc} = 0$: $3.5 < \Gamma < 7 - 9$; small aspect ratios (S);
- $N_{lc} > 1$ and $N_{cc} = 1$: $7 < \Gamma < 9$; small-to-medium aspect ratio transition (StM);
- $N_{cc} > 1$ and $N_{cc}/N_{lc} \approx 1$: $7 - 9 < \Gamma < 30 - 40$; medium aspect ratios (M);
- $N_{cc}/N_{lc} >> 1$: $30 - 40 < \Gamma$; large aspect ratios (L).

4 Beyond the threshold

As the Marangoni number is increased above the threshold one can encounter a secondary bifurcation that corresponds to not only a pattern change but also a slope change in the Nusselt number plot. Moreover, we checked that different initial conditions lead to the same pattern. Depending on the (ε, Γ) set we have encountered either steady state or dynamical configurations, even for small values of $\varepsilon < 0.2$, $\varepsilon = (Ma - Ma_c)/Ma_c$, Ma_c critical Marangoni number for the container considered.

4.1 Steady states

We have studied supercritical regimes according to [14] up to the second bifurcation, plotted in Figs. 2a–e (bold symbols) along with their corresponding patterns (upper row). In spite of the container shape diversity it can be seen that all patterns display a similar evolution as Γ increases: i) for very small Γ only one cell exists, which has necessarily the container shape; ii) for $3.5 < \Gamma < 7 - 9$, several lateral-cells (lc), made up of tetragons or pentagons, in contact with the container walls exist; iii) going further, for $\Gamma \approx 7 - 9$ depending on the vessel shape, one central-cell appears, whose shape depends on the container geometry. The shape of central-cell is much less constrained by the container shape than the lateral-wall-cells. Hence this central-cell is very likely to be a somewhat regular polygon, whereas the lateral-cells are in turn very likely to become of pentagonal shape. However one can notice that the first core-cell (cc) appears for smaller Γ in CVs than in ICVs. iiii) beyond this aspect ratio transition ($\Gamma \approx 7-9$) because the number of core cells increases faster than the number of lateral cells, the higher the aspect ratios, the less geometrically constrained the core-cells by the lateral walls. Then the first central-cell is replaced by polygonal cells; iiiii) finally any further increase in the aspect ratio, provided it satisfies a geometrical compatibility rule (hereafter designated "size-length condition") produces an internal

core of hexagonal cells, surrounded with a belt of lc. Concerning the patterns one can observe that they only keep the container symmetries in P_3. Otherwise one observes a two or four-fold symmetry for P_4, two or five-fold for P_5, two, three or six-fold for P_6. Finally for P_∞ all the symmetries have been displayed from two-fold up six-fold (where n-fold corresponds to a $2\pi/n$ symmetry).

Let us now move to some new specific behaviours that have not been reported yet, although they present some interesting features. Considering CVs (i.e. P_3 and P_6) a regular hexagonal pattern is obtained in the core region provided the vessel lateral-wall length satisfies the size-length condition, even from Γ as small as $\Gamma = 6.45$ in P_6. Moreover, if the container diameter fits an odd number times the intrinsic wavelength of the hexagonal-cell pattern, then the hexagonal symmetry is fully recovered. Conversely, a two-fold symmetry can be observed and the central hexagonal-cells could be slightly distorted. On the other hand, very small (less than 3% of the free surface area) motionless wedge-cells appear for small Γ in P_3, owing to high shear stress in these zones. For the ICV P_4 and for $\Gamma < 9$ some comparisons with experiments [14] have been previously reported [16]. The computed weakly supercritical patterns correspond to those that were instead attributed by the former authors as patterns at threshold. For $\Gamma > 9$ we considered three other vessels that satisfy the size length condition: in these cases a square pattern can exist. On the opposite for $\Gamma = 22$, which does not satisfy this condition, a disordered pattern is observed. For P_5, the second ICV, the hexagonal pattern can only be observed for the second bifurcation and large Γ ($\Gamma = 22.16$). For circular containers most of the lowest aspect ratios were chosen for comparison purpose with previous experimental works [14]. Here again, our weakly supercritical patterns correspond to their patterns attributed at threshold. Although the circular vessel is not compatible with respect to the hexagonal pattern, one can nevertheless achieve a length-size compatibility condition, which enables us to perform quasi-regular hexagonal patterns for several aspect ratios.

4.2 Dynamical regimes

Rotating patterns are known in circular vessels [6,13] while oscillating patterns have been observed in square vessels [19]. But we have found that dynamical regimes can be encountered in most of the very-small and small aspect ratio configurations. We present in Figs. 3a–d a few typical characteristic behaviours: cell pulsation, pattern rotation and deformation, combination of both mechanisms. Rotating and oscillating patterns have been observed in a P_∞ with $\Gamma = 4.71$ (Fig. 3a) and P_6 with $\Gamma = 4.84$ (Fig. 3b), respectively. Both patterns have a similar behaviour: the vessels contain two cells at the second bifurcation ($Ma = 1.03Ma_c$ and $Ma = 1.25Ma_c$, respectively) which become unstable at $Ma \approx 1.4Ma_c$ and $Ma \approx 1.5Ma_c$, respectively, and give rise to a periodic dynamical regime. In the cylinder this azimuthal motion results in a continuous and uniform revolution of the whole structure, with a dimensionless rotating period of $Ta = 106.6$ at $\varepsilon = 0.25$. In the P_6 a periodic oscillation of $\pm\pi/6$ appears with a dimensionless period of $Tb = 181.6$ at $\varepsilon = 0.6$.

In the P_4 container ($\Gamma = 9.75$) the pattern is made up of nine identical square cells at the secondary bifurcation ($Ma = 1.16Ma_c$, Fig. 3d) and becomes unstable at $Ma \approx 1.7Ma_c$. The instability develops first in a pulsating mode in the cells, the central one being in opposite phases with respect to its first four neighbouring cells. As far as the magnitude of the pulsation reaches a critical value a periodical oscillation and distortion of the central cell take place and superimpose on the pulsating movement. The corresponding dimensionless period is $Td = 25$ at $\varepsilon = 0.7$.

The pattern in P_5 container ($\Gamma = 4.16$) is made up of twin-cells at threshold, but here the cell number evolves in the course of time from one to three cells (Fig. 3c).
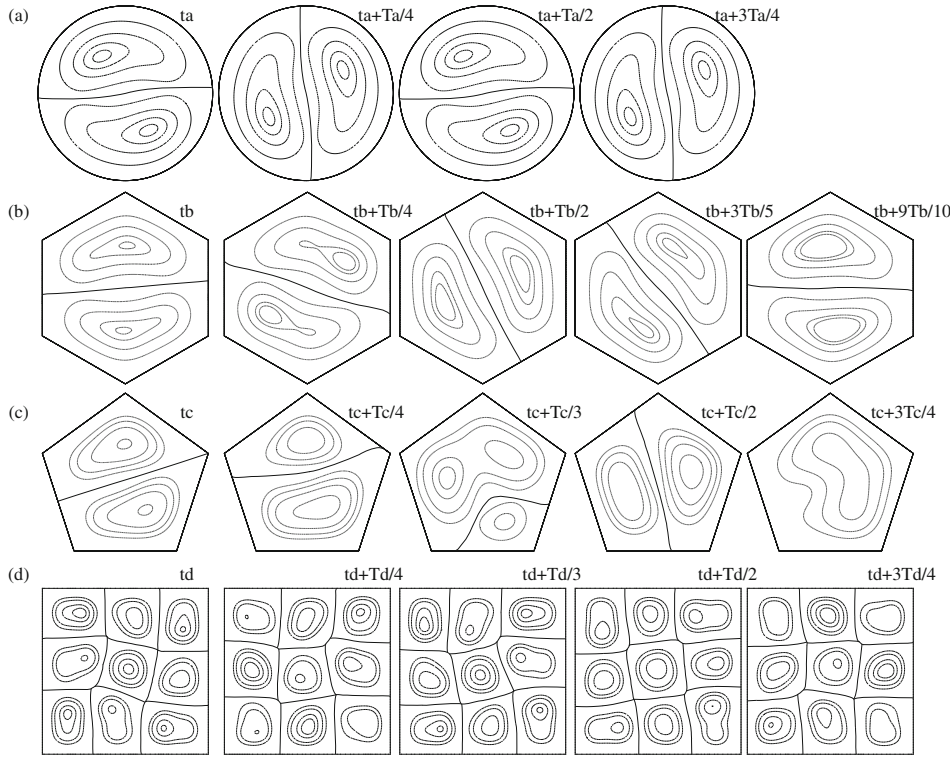
Fig. 3. Samples of dynamical patterns computed in some regular polygonal and circular containers close to the threshold ($Pr = 900$, $Bi = 0.1$); ti and Ti represent the time and period of case $i = a$–d, respectively; (a) circular: $Ta = 106.6$, $\varepsilon = 0.25$; (b) hexagonal: $Tb = 181.6$, $\varepsilon = 0.6$; (c) pentagonal: $Tc = 190$, $\varepsilon = 0.8$; (d) square: $Td = 25$, $\varepsilon = 0.7$.

This pattern becomes unstable for $Ma \approx 1.65 Ma_c$ through a pulsating mode in which the two cells pulsate in opposite phases. Beyond a critical size the bigger cell splits in two parts, which grow first in the same way provoking the disappearance of the third cell. Then, one of them takes place in the facing wedge whereas the other one lies in the wider left area. The wider cell expands to the detriment of the smaller one, which progressively disappears while the wider splits at its turn in two parts and the cycle repeats again. The corresponding dimensionless period is $Tc = 190$ at $\varepsilon = 0.8$.

5 Analysis and discussion

We address the main underlying point on how much do the container size and shape quantitatively influence the convective fluid flow characteristics. Let us start our analysis with the mechanisms at play at threshold in very small Γ ($\Gamma < 3.5$) where only one convective cell takes place. Let us define a relative friction coefficient for each vessel, which compares the driving free surface area (A) to the total friction one ($A + p\,d_l$, where p is the wetted vessel perimeter and d_l is the liquid layer depth): $f = (A + p\,d_l)/A = 1 + C_n/\Gamma$, where C_n is a geometrical constant, which only depends on the vessel shape. Figure 1b plots ε_Γ versus f for $Pr = 900$ and $Bi = 0.1$, where $\varepsilon_\Gamma = (Ma_c - Ma_{c\infty})/Ma_{c\infty}$, for a vessel of aspect ratio Γ), from which it is clearly shown that for $f \approx 2-3$ all vessels have the same ε_Γ for a given f. So it turns out that

threshold values in very small aspect ratio vessels are mainly ruled by the relative friction coefficient, which depends on both vessel size and shape. It can be concluded from Figs. 1 and 2 that three zones can be distinguished owing to the leading mechanisms: i) for $\Gamma < 3.5$ threshold values are ruled by relative friction coefficient; ii) for $3.5 < \Gamma < 10 - 15$ threshold is mainly ruled by vessel size and more weakly by its shape; iii) for $\Gamma > 10 - 15$ threshold value tends asymptotically towards the infinite layer limit. For a given Γ the friction area diminishes as the number of regular polygon sides increases, up to the ultimate infinite value for the circular shape. On the other hand, wedge influence in regular polygons scales as $1/n$ (n wedge number). Therefore, taking into account these two effects let us introduce the following expression:

$$\varepsilon_\Gamma = \frac{a + c/n}{\Gamma} + b + d/n \tag{4}$$

where $3 < n < \infty$ and a, b, c, d four constants (2.9; -0.2; 7; -0.35), which fairly reproduces the general trend for very small aspect ratios within less than 2% discrepancy on Ma_c, see Fig. 1a. This scaling law enables to estimate threshold value for containers of any regular shape in the very-small aspect ratio range for the Pr and Bi considered.

Let us consider to the confinement influence in a pattern made up of many cells. All experiments and numerical simulations show that boundaries between adjacent cells lying along vessel walls are roughly perpendicular to them. That is the reason in which originates the distinction between CVs and ICVs (geometrical condition). Moreover, as soon as a hexagonal pattern appears it tends to get its intrinsic size, which is that of the unbounded pattern (hydrodynamical condition). However the pattern confined in a container only tolerates cell-widths within an admissible bandwidth ($\pm 6\%$) [3] (size condition). It has been observed that this bandwidth decreases as Γ increases and is greater for ICVs than for CVs. For P_6 and P_∞ it is for a hexagonal central cell $\pm 1\%$, which roughly corresponds to the infinite layer pattern cell width. So, one can conclude that P_∞ behaves as a CV in the central part of the vessel, what that formerly assumed by Bénard [1]. Furthermore, we have also observed that lateral cells possess larger admissible deformation than core cells.

Let us finally discuss the existence of steady state or dynamical patterns. The latter recurrently appeared much closer to the threshold in most of very small aspect ratio configurations compared to previous works [11,15,19]. The spatially resonant pattern [6,11] originates in the difference between intrinsic cell-size for the considered ε and that imposed by the container. So, when the constrained pattern fits both admissible bandwidth-size of the core cells and admissible "elasticity" of lateral cells, then a steady state pattern can exist. Otherwise, a dynamical regime will emerge even very close to the threshold. Dynamical regimes in small vessels and close to the threshold can be explained theoretically by the existence of a co-dimensional two-points [6,13]. On the other hand, computations have shown that the border shape between two cells depends on their relative kinetic energy: it is a straight line if they have the same energy and otherwise its concavity is towards the cell of highest energy. When two neighbouring cells have the same energy, but different spatial distribution their interface takes an S shape. This distorsion induces either a rotating (in P_∞) or oscillating (in P_6) pattern that evolves in time from the concave to the convex region. On the other hand when kinetic energy increases in a cell, its size increases accordingly at the detriment of neighboring cells of lower kinetic energy up to a critical limit, where this coarsening cell splits in two parts. This results in the "birth" of a new cell and consequently to a dynamical pattern [22], which takes place whatever Γ is. So, dynamical regimes seem to be an intrinsic $STDBC$ behavior in the strongly confined configurations, since it happens whatever the vessel shape is and even close to the threshold.

6 Conclusion

The container size and shape influences on both threshold and its associated pattern, together with weakly supercritical regime up to the secondary bifurcation ($\varepsilon < 2$) are studied in $STDBC$ for high Prandtl number ($Pr \approx 900$). Five container shapes of various sizes, in the very small-to-moderate aspect ratio range ($2 \leq \Gamma < 24$) have been considered and their respective convective characteristics (threshold, pattern) were compared. These results are the first ones ever obtained in P_3, P_5 and P_6 containers along with original ones in P_4 and P_∞, according to the authors' knowledge. Indeed, in the latter case, some patterns have been found to correspond to the secondary bifurcation despite they were formerly attributed to threshold in experimental works [14]. Furthermore, to unify the denominations among authors we have introduced a classification of container sizes according to the convective structure. For $\Gamma < 3.5$ the threshold value depends only on the friction coefficient, whereas for larger aspect ratios it depends only on Γ and for $\Gamma > 10 - 15$ it tends towards the infinite layer limit. Concerning the pattern in small aspect ratios, steady state solutions only exist if a size compatibility condition is satisfied, whereas otherwise periodical regime appears even very close to the threshold. This feature is an intrinsic $STDBC$ behaviour, since it appears in all the container shapes considered. Moreover various modes can be observed depending on the container shape: rotating, pulsating and mixed mechanisms in spatially resonant patterns (co-dimension-two points). On the other hand, some containers are more likely to induce a perfect hexagonal pattern than any others provided they satisfy both the geometrical condition (compatible vessels: P_3 and P_6) and the size compatibility one (hydrodynamical condition). Hence configurations of quasi-perfect hexagonal pattern in the core region can be devised at wish, even in moderate aspect ratios, as they reproduce the infinite layer features. This study could be extended in several promising directions: i) characterization of the bifurcation nature at threshold according to the vessel shapes and sizes; ii) examination of higher distances from the threshold in which interesting steady state pattern transitions occur.

Appendix

A summary of the studied geometrical configurations is listed in Table A1. Meshes used in computations are reported in Table A2. A unit generic mesh has been built for each shape and a conformal mapping onto the nodal coordinates of the generic root mesh has been performed to match prescribed aspect ratios.

Table A1. Considered aspect ratios: a) P_3; b) P_4; c) P_5; d) P_6; e) P_∞ containers.

a)	2.0	2.5	3.0	3.5	4.0	5.0	6.3	8.5	11.4	12.2	15.1	17.1	22.0
b)	2.0	2.5	3.0	3.5	4.0	5.68	6.18	6.36	8.48	9.75	13.0	16.25	22.0
c)	2.0	2.5	3.0	3.5	4.0	4.63	6.17	7.71	8.48	9.25	13.42	18.5	23.6
d)	2.0	2.5	3.0	3.5	4.0	4.84	6.45	8.38	11.28	14.1	16.92	19.75	22.36
e)	2.0	2.5	3.0	3.5	4.0	4.71	5.84	6.02	7.64	7.94	8.27	16.23	22.16

Table A2. Computational meshes used for each container shape.

Computational domain shape	# of H27 finite elements horizontal plane × depth	# of Mesh nodes horizontal plane x depth
Triangular	2187×10	8911×21
Square	2500×10	10201×21
Pentagonal	2205×10	9031×21
Hexagonal	2187×10	8911×21
Circular	2016×10	8209×21

References

1. H. Bénard, Rev. Gén. Sci. Pures Appl. **11**, 1261 (1900)
2. P. Cerisier, C. Perez-Garcia, C. Jamond, J. Pantaloni, Phys. Rev. A. **33**, 1949 (1987)
3. P. Cerisier, M. Zouine, Phys. Chem. Hydrodyn. **11**, 659 (1989)
4. B. Cochelin, M. Medale, J. Comput. Phys. **236**, 594 (2013)
5. P. Colinet, J.C. Legros, M.G. Velarde, *Nonlinear Dynamics of Surface-Tension-Driven Instabilities* (Wiley-VCH, 2001)
6. P.C. Dauby, P. Colinet, D. Jonhson, Phys. Rev. **61**, 2663 (2000)
7. P.C. Dauby, G. Lebon, J. Fluid Mech. **329**, 25 (1996)
8. P.C. Dauby, G. Lebon, E. Bouhy, Phys. Rev. E. **56**, 520 (1997)
9. H.A. Dijkstra, J. Fluid Mech. **243**, 73 (1992)
10. H.A. Dijkstra, Microgravity Sci. Technol. **8**, 155 (1995)
11. B. Echebarria, D. Krmpotic, C. Perez-Garcia, Physica D: Nonlinear Phenom. **99**, 487 (1997)
12. K. Eckert, M. Bestehorn, A. Thess, J. Fluid Mech. **356**, 155 (1998)
13. D. Jonhson, R. Narayanan, Phys. Rev. E. **54**, R3102 (1996)
14. E.L. Koschmieder, S.A. Prahl, J. Fluid Mech. **215**, 571 (1990)
15. H.L. Mancini, D. Maza, Phys. Rev. E. **55**, 2757 (1997)
16. M. Medale, P. Cerisier, Num. Heat. Trans. A. **42**, 55 (2002)
17. M. Medale, B. Cochelin, J. Comp. Phys. **228**, 8249 (2009)
18. A.A. Nepomnyahchy, M.G. Velarde, P. Colinet, *Interfacial Phenomena and Convection.* Monographs and Surveys in Pure and Applied Mathematics 124 (Chapman & Hall/CRC, 2002)
19. T. Ondarçuhu, G. Mindlin, H.L. Mancini, C. Perez-Garcia, Phys. Rev. Lett. **70**, 3892 (1993)
20. A. Thess, S.A. Orszag, J. Fluid Mech. **283**, 201 (1995)
21. H. Tomita, K. Abe, Phys. Fluids **16**, 1389 (2000)
22. A. Wierschem, P. Cerisier, P. Gallet, M. Velarde, J. Non-equilib. Thermodyn. **22**, 162 (1997)
23. K.H. Winters, T. Tesser, K.A. Cliffe, Physica D. **30**, 387 (1998)
24. A. Zaman, R. Narayanan, J. Colloid Interface Sci. **179**, 151 (1996)